Impact of submicron Nb_3Sn stoichiometric surface defects on high-field superconducting radiofrequency cavity performance

Sarah A. Willson,[1,*,†] Aiden V. Harbick,[2,*] Liana Shpani,[3] Van Do,[1] Helena Lew-Kiedrowska,[1] Matthias U. Liepe,[3] Mark K. Transtrum,[2] and S. J. Sibener[1,‡]

[1]*The James Franck Institute and Department of Chemistry, The University of Chicago, 929 E. 57th Street, Chicago, Illinois 60637, USA*

[2]*Department of Physics and Astronomy, Brigham Young University, Provo, Utah 84604, USA*

[3]*Cornell Laboratory for Accelerator-Based Sciences and Education, Cornell University, Ithaca, New York 14853, USA*

(Received 3 July 2024; accepted 8 October 2024; published 13 November 2024)

Nb_3Sn film coatings have the potential to drastically improve the accelerating performance of Nb superconducting radiofrequency (SRF) cavities in next-generation linear particle accelerators. Unfortunately, persistent Nb_3Sn stoichiometric material defects formed during fabrication limit the cryogenic operating temperature and accelerating gradient by nucleating magnetic vortices that lead to premature cavity quenching. The SRF community currently lacks a predictive model that can explain the impact of chemical and morphological properties of Nb_3Sn defects on vortex nucleation and maximum accelerating gradients. Both experimental and theoretical studies of the material and superconducting properties of the first 100 nm of Nb_3Sn surfaces are complicated by significant variations in the volume distribution and topography of stoichiometric defects. This work contains a coordinated experimental study with supporting simulations to identify how the observed chemical composition and morphology of certain Sn-rich and Sn-deficient surface defects can impact the SRF performance. Nb_3Sn films were prepared with varying degrees of stoichiometric defects, and the film surface morphologies were characterized. Both Sn-rich and Sn-deficient regions were identified in these samples. For Sn-rich defects, we focus on elemental Sn islands that are partially embedded into the Nb_3Sn film. Using finite element simulations of the time-dependent Ginzburg-Landau equations, we estimate vortex nucleation field thresholds at Sn islands of varying size, geometry, and embedment. We find that these islands can lead to significant SRF performance degradation that could not have been predicted from the ensemble stoichiometry alone. For Sn-deficient Nb_3Sn surfaces, we experimentally identify a periodic nanoscale surface corrugation that likely forms because of extensive Sn loss from the surface. Simulation results show that the surface corrugations contribute to the already substantial drop in the vortex nucleation field of Sn-deficient Nb_3Sn surfaces. This work provides a systematic approach for future studies to further detail the relationship between experimental Nb_3Sn growth conditions, stoichiometric defects, geometry, and vortex nucleation. These findings have technical implications that will help guide improvements to Nb_3Sn fabrication procedures. Our outlined experiment-informed theoretical methods can assist future studies in making additional key insights about Nb_3Sn stoichiometric defects that will help build the next generation of SRF cavities and support related superconducting materials development efforts.

DOI: 10.1103/PhysRevResearch.6.043133

I. INTRODUCTION

Extensive resources and research personnel have been put towards optimizing the accelerating gradients in accelerator and high energy collider facilities, such as the LCLS-II at SLAC National Laboratory [1]. Current state-of-the-art linear accelerators utilize niobium (Nb) superconducting radiofrequency (SRF) cavities, enabling 30–35 MV/m gradients with quality factors (Q) of $\sim 10^{10}$ while operating at $\sim$2 K [2–4]. To reduce this cryogenic burden, thereby increasing the accessibility of SRF technology, the accelerator physics community has been exploring alternative SRF materials that can enhance cavity accelerating gradients and Q factors while enabling SRF operation above 4 K. One such potential next-generation SRF material is the $A15$ triniobium-tin alloy (Nb_3Sn), which has a higher critical temperature T_c ($\sim$18 K) and superheating field ($\mu_0 H_{sh}$: 425 mT) than elemental Nb ($T_C \sim 9$ K, $\mu_0 H_{sh}$: 220 mT). Coating the interior walls of an existing Nb SRF cavity with a thin Nb_3Sn film could theoretically enable accelerating gradients as high as $\sim$100 MV/m while operating above 4 K ($Q \sim 10^{10}$) [5].

However, Nb_3Sn-coated SRF cavities have only achieved gradients of 24 MV/m to date [6], underperforming the elemental Nb cavities. The poor SRF performance of Nb_3Sn is attributed to material defects accrued within the films during the standard Sn vapor diffusion growth procedure. Despite the Sn vapor diffusion procedure producing the highest

*These authors contributed equally to this work.

†Present address: KLA, 1 Technology Drive, Milpitas, CA 95035, USA.

‡Contact author: s-sibener@uchicago.edu

performing cavity coatings, the small coherence length (∼4 nm) of Nb_3Sn means that its superconducting behavior is particularly sensitive to material defects, which include regions with inconsistent film growth, stoichiometric deficiencies, and surface roughness [7–13]. Nb_3Sn coatings formed on Nb SRF surfaces exhibit structural and chemical Nb_3Sn inhomogeneities. Combined with the brittleness of the alloy and other practical challenges of growing a high-quality Nb_3Sn film, these inhomogeneities have, to date, limited the use of Nb_3Sn in high-field accelerator applications [14].

Numerous growth studies of the Sn vapor diffusion procedure have resulted in improvements to the material properties of formed Nb_3Sn coatings. One such area of improvement has been identifying that the relatively slow Sn diffusion through Nb_3Sn bulk, as compared to Sn diffusion through Nb_3Sn grain boundaries, results in Sn deficiencies preferentially forming in larger Nb_3Sn grains. Sn-deficient regions of the $A15$ lattice manifest as antisite defects and can lower the Sn atomic percent (at.%) to as low as 18% [10,14]. Cross-sectional energy dispersive spectroscopy (EDS) maps have documented Sn-deficient regions throughout the entirety of the Nb_3Sn film, particularly at the interior of large grains and at the intermetallic interface [7,15–17]. Procedural changes to the vapor deposition procedure, such as increasing the Sn vapor pressure, have been effective in decreasing the incidence of larger, Sn-deficient Nb_3Sn grains [6,18].

While the Nb_3Sn grain sizes are driven by the experimental conditions during nucleation and coating steps, it is the cooldown procedure that primarily dictates the stoichiometry and roughness in the first few nanometers of the films. The Nb_3Sn film surface is particularly prone to forming chemical deviations, such as Sn-rich residues, that likely impact the cavity Q factors [19,20]. However, we lack a thorough experimental realization of how stoichiometric defects form, specifically at the Nb_3Sn surface, where Sn-rich and Sn-deficient regions can form with larger volumes and alter the roughness and morphology of the Nb_3Sn surface. One contribution to the lack of experimental data on chemical defects in the Nb_3Sn surface region is the barriers to experimentally characterizing Nb_3Sn surfaces with surface (<100 nm), spatial (lateral), and chemical sensitivity. To visualize and characterize Nb_3Sn surfaces, spectroscopic tools such as EDS provide chemical contrast information, but lack the spatial (lateral and depth) resolution to accurately probe nanometer-scale surface features. Depending on the electron beam energy and the sample properties, probed x rays used during EDS measurements can originate from hundreds of nanometers below the surface [21]. Alternatively, x-ray photoelectron spectroscopy (XPS) has higher surface sensitivity, usually on the order of nanometers. However, XPS instruments do not typically focus the photon beam to achieve any lateral spatial resolution. Another issue is that XPS measurements can suffer poor quantitative accuracy due to the surface roughness, heterogeneities, and oxidative properties of Nb_3Sn surfaces [22,23]. EDS, XPS, and other common structural analysis tools such as x-ray diffraction (XRD), provide valuable information about the ensemble Nb_3Sn film properties, but lack the lateral and surface sensitivity to examine the volume and geometric distribution of nanometer-scale surface defects. This can result in stoichiometric defects, such as ∼10-nm Sn islands on a Sn-deficient Nb_3Sn surface, being experimentally characterized as near-stoichiometric 25 at.% Sn. To fully capture chemical deviations at both nanometer and micron scales, it may be beneficial to shift the focus to experimentally probing the Nb_3Sn grain morphology rather than solely relying on global chemical analysis to infer the local chemistry at the film surface. For example, large grains with uncharacteristically low surface roughness are almost always Sn deficient. This means that upon observing such grains in future measurements, they can initially be assumed to be Sn deficient. In this sense, experimental observations can alleviate some of the challenges associated with accurately quantifying spectroscopic data. Relating Nb_3Sn surface chemistry with microscopic features can reduce the barriers associated with assessing the Nb_3Sn film's material properties and, ultimately, the SRF performance.

Because of the large variety of geometric and stoichiometric defects that can be present in Nb_3Sn surfaces, and the difficulties associated with experimentally probing local microscopic features, numerical simulation of superconducting fields in the presence of these features can play a powerful role in understanding their impact on SRF performance. Among the most useful outputs of these simulations is the estimation of critical fields for hypothetical Nb_3Sn surfaces. Nb_3Sn is a type-II superconductor, so it has a stable mixed state between its lower and upper critical fields (H_{c1}, H_{c2}) in which magnetic flux vortices can penetrate the surface. These vortices dissipate energy as they are driven by the rf cycle, which degrades SRF cavity quality factors and, in some cases, leads to thermal runaway and cavity quenching (i.e., transitions to normal conducting). However, the lower critical field is not the threshold for vortex nucleation. In practice, an energy barrier against vortex nucleation allows the superconducting (Meissner) state to remain metastable up to the superheating field, H_{sh}, at which point the energy barrier disappears. Above H_{sh}, vortex nucleation is unavoidable, and so the superheating field is the fundamental limit for the maximum accelerating gradient of an SRF cavity. High-field Nb SRF applications are known to operate above H_{c1}, within the metastable Meissner regime [24]. Nb_3Sn cavities, with a lower critical field of ∼38 mT [25], also operate in the metastable state when accelerating gradients exceed ∼9 MV/m. In this state, SRF performance is especially sensitive to material defects that can act as vortex nucleation sites. Because of this, the performance of Nb_3Sn SRF cavities is determined by local stoichiometric and geometric features present in the first few hundred nanometers of the surface. Previous literature demonstrated a strong effect of varying the global Sn percentage on the calculated and measured T_c [5,26]. Additionally, several theoretical studies have investigated the surface topography and Sn volume distribution of Sn-segregated grain boundaries and their superconducting properties [8,27]. However, the lack of predictive modeling limits our ability to connect the wide variety of Sn volume distributions and feature geometries in realistic Nb_3Sn surfaces to specific performance metrics.

We present herein a broad experimental and theoretical investigation of how certain structural variations of Sn-rich and Sn-deficient Nb_3Sn surfaces form during sample growth and their potential impact on SRF performance metrics. In particular, we look at the formation and impact of Nb_3Sn

surfaces which are Sn rich due to Sn islands, and the large, flat, Sn-deficient grains and the nanometer-scale corrugations that appear on them. Vapor-deposited Nb_3Sn films were formed both in an ultrahigh-vacuum (UHV) chamber and in a cavity-coating furnace. Experimental data provide insight into how the critical final cooldown steps of the Nb_3Sn growth procedure can drastically alter the surface stoichiometry, geometric distribution, and topographical profile of nonstoichiometric Nb_3Sn species. These experimental characterizations are modeled as approximate Nb_3Sn surface profiles. Simulation of these profiles shows how realistic surface features alter the critical fields and vortex nucleation behavior of the underlying material. In this way, this study demonstrates how structural and stoichiometric properties in observed surface defects can contribute to decreases in the maximum accelerating gradient of Nb_3Sn-coated SRF cavities.

The paper is outlined in the following order. The Methods section (Sec. II) contains a subsection devoted to the experimental methods (Sec. II A). The UHV Nb_3Sn growth and *in situ* characterization procedures, as well as the furnace Nb_3Sn growth procedure are outlined in Secs. II A 1 and II A 2, respectively. Section II A 3 details the experimental *ex situ* film characterization methods. The theoretical methods are discussed in Sec. II B. The Results and Discussion section (Sec. III) is comprised of three subsections (Secs. III A–III C), each containing an experimental and theory-based component to comprehensively characterize Nb_3Sn surfaces for high-field SRF performance. Section III A outlines the challenges associated with assessing how the Nb_3Sn surface morphology impacts SRF performance from experimental and theory-based perspectives. Section III A 1 outlines how experimental growth conditions can impact the Nb_3Sn stoichiometry throughout the entire film and at the surface. This section also discusses the challenges associated with characterizing the Nb_3Sn Sn at.% using commonly available techniques. In Sec. III A 2, the calculated relationship between the superheating field and the global Nb_3Sn stoichiometry is discussed. In Sec. III B, the formation and superconducting properties of Sn-rich Nb_3Sn surfaces, particularly Sn islands, are described. Finally, Sec. III C addresses the surface morphology and impact of Sn-deficient surfaces on SRF performance.

II. METHODS

A. Experimental methods

1. *UHV film growth and in situ characterization (Recipes 1 and 2)*

Nb_3Sn films were grown in a UHV chamber equipped with an electron beam evaporator (EFM3T; Focus GmbH) containing a tantalum crucible containing Sn pellets [Fig. 1(a)]. The substrate was a polycrystalline Nb foil (99.9% purity; Goodfellow) that did not undergo any mechanical polishing. Before Sn deposition, the Nb foil underwent repeated Ar^+ sputtering (1.5 keV) and annealing (T_{anneal}: 1630 °C) cycles to form an ordered NbO surface free of carbon contamination. The Nb surface composition was assessed with *in situ* XPS and Auger electron spectroscopy (AES). A 3.00 keV electron source (Staib) was used in AES and a Mg $K\alpha$ photon source (Specs XR 50) was used for XPS. Both AES and

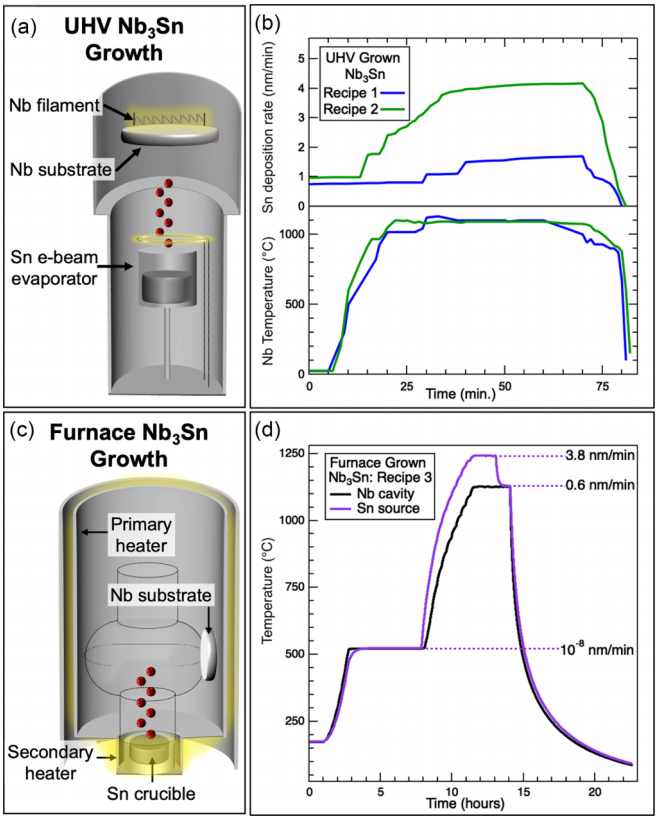

FIG. 1. Three different growth recipes used to form the Nb_3Sn films on Nb substrates. Schematics of experimental setups for (a) e-beam and (c) furnace deposition; (b) e-beam growth conditions for Nb_3Sn film Recipes 1 and 2; (d) furnace temperatures for Nb_3Sn film Recipe 3.

XPS photoelectron signals were collected using a cylindrical mirror analyzer (Staib DESA 100). The sampling depth for the Mg $K\alpha$ anode (1253.6 eV) in this setup is approximately 6 nm, whereas the sampling depth (3λ) for our Auger beam is approximately 2 nm [22].

Preceding Sn deposition, the Nb sample was sputtered with 1.5 keV Ar^+ for 15 min at room temperature to increase the density of favorable Sn nucleation sites on the Nb surface [28,29]. The base pressure in the deposition chamber was approximately 10^{-9} torr. During evaporation, the Nb and Sn temperatures were independently controlled using two separate filaments [Fig. 1(a)]. Since the Nb substrate and Sn source were electron beam annealed, the temperatures were able to rapidly quench during the final cooldown steps of the deposition procedure [Fig. 1(b)]. The Nb temperature was monitored using an infrared pyrometer (Mikron Infrared; MG-140). The Sn flux at the substrate in nm/min was found by calibrating the evaporator heating conditions with a quartz crystal microbalance (QCM; INFICON) that was inserted into the same position as the Nb sample during deposition. A summary of the growth recipes used to experimentally grow each Nb_3Sn film can be found in Table I.

Recipes 1 and 2 are the UHV-grown Nb_3Sn films grown at the University of Chicago and were intended to represent condensed versions of the standard Nb_3Sn vapor deposition procedure [6]. The Nb heating conditions were comparable

TABLE I. Preparation of different Nb_3Sn surfaces.

Growth recipe	Deposition environment	Peak T_{Nb}	Peak T_{Sn}	Peak Sn deposition rate	Cooldown period (starting from T_{Nb}: 1100 °C)	Estimated film thickness
1	UHV	1100 °C	1120 °C	1.7 nm/min	<2 min	∼275 nm
2	UHV	1100 °C	1175 °C	4.2 nm/min	<20 min	∼500 nm
3	Furnace	1130 °C	1243 °C	3.8 nm/min	7 h	∼3 μm

for both growth recipes (peak T_{Nb}: 1100 °C). For Recipe 1, the Sn flux was kept intentionally low (peak: 1.7 nm Sn/min) in order to promote the growth of large Sn-deficient grains [30]. For Recipe 2, the Sn flux was higher (peak: 4.2 nm Sn/min) to better simulate the typical Sn impingement rate in the standard Nb_3Sn procedure. In the typical growth furnace, the Sn flux is highly dependent on the location of the Nb cavity with respect to the Sn source, so Recipes 1 and 2 represent how deposition conditions can vary across the Nb SRF cavity surface [30,31]. The main differences from the furnace growth procedure in Recipes 1 and 2 are the shorter growth time, smaller film thickness, and the lack of a $SnCl_2$ nucleating agent during the initial nucleation growth step [hours 2–8 in Fig. 1(d)]. The $SnCl_2$ increases the Sn vapor pressure during the nucleation stage since the Sn source is only at ∼525 °C. To compensate, the UHV-grown films had a relatively consistent Sn flux throughout the entire growth procedure. In the Supplemental Material [32], the Sn source temperatures during Recipes 1 and 2 were calculated from the deposition rate and plotted in Fig. S1(a) [33,34].

2. *Furnace film growth (Recipe 3)*

The Recipe 3 film was prepared using the standard vapor diffusion recipe at Cornell University [35]. High residual resistivity ratio (RRR) niobium samples were electropolished before being placed in the high-vacuum vapor diffusion furnace. The samples were hung from the heat shields to a height of where the equator of a 1.3-GHz cavity would be relative to the Sn source. After degassing the furnace at ∼175 °C, the Nb temperature was ramped up to the nucleation temperature of ∼500 °C and held there for 5 h. During this time, Sn-rich droplets started to nucleate on the Nb substrate. Utilizing the secondary heater for the Sn source, a temperature gradient of ∼170 °C was established before ramping the temperature up for the coating stage. During the coating stage, the temperature of the Sn source was kept at ∼1200 °C, while the samples were kept at ∼1100 °C for 1.5 h. Lastly, the secondary heater was turned off, and the samples were annealed at 1100 °C for 1 h.

The Sn deposition rates used during Recipe 3 were calculated from the measured temperature of the Sn source during growth and plotted in Fig. S1. Nb_3Sn films were transported to the University of Chicago for analysis.

3. *Ex situ film characterization*

Scanning electron microscopy (SEM; Zeiss Merlin), EDS (Oxford Ultim Max 100), atomic force microscopy (AFM; Asylum Research Cypher), and XRD (Rigaku SmartLab) measurements were taken *ex situ*. SEM images were acquired using the Everhart Thornley secondary electron (SE), In-lens SE, In-lens, and angle selective backscatter (AsB) detectors. SEM characterization was conducted with a primary beam energy between 1 and 10 keV depending on the desired surface sensitivity and selected detector. The typical primary beam current was 5 nA for all images except for those taken with a 1-kV beam voltage, in which the beam current was lowered to 1–3 nA. Surface topography measurements were conducted using AFM. Images were taken on an atomic force microscope in tapping mode. All image workup and analysis was conducted using GWYDDION, an image analysis software. XRD measurements with taken using Cu $K\alpha$ radiation (1.54 Å).

The Nb_3Sn stoichiometry of each film was assessed with EDS and XRD. During EDS measurements, the primary beam was kept at 7 kV for the films grown with Recipes 1 and 2 and increased to 10 kV for the thick film grown with Recipe 3. The Nb_3Sn films grown using Recipes 1 and 2 are approximately between 250 and 500 nm thick, so EDS measurements were taken at the lowest possible beam energy to increase the surface sensitivity without comprising the EDS energy resolution [21]. It is still possible that the EDS signal probed past the intermetallic Nb_3Sn/Nb interface for these thinner films, so the EDS measurements likely underestimated the Sn concentration in the Recipe 1 and 2 Nb_3Sn films.

B. Theoretical methods

The simulations in this paper were done using the time-dependent Ginzburg-Landau (TDGL) equations,

$$\Gamma\left(\frac{\partial\psi}{\partial t}+\frac{ie_s\varphi}{\hbar}\psi\right)+\frac{1}{2m_s}\left(-i\hbar\nabla-\frac{e_s}{c}\boldsymbol{A}\right)^2\psi + \alpha\psi+\beta|\psi|^2\psi=0, \tag{1}$$

$$\frac{4\pi\sigma_n}{c}\left(\frac{1}{c}\frac{\partial\boldsymbol{A}}{\partial t}+\nabla\varphi\right)+\nabla\times\nabla\times\boldsymbol{A} - \frac{2\pi ie_s\hbar}{m_sc}(\psi^*\nabla\psi-\psi\nabla\psi^*)+\frac{4\pi e_s^2}{m_sc^2}|\psi|^2\boldsymbol{A}=0. \tag{2}$$

These equations (presented here in Gaussian units) are solved for the complex superconducting order parameter, ψ, and the magnetic vector potential, $\boldsymbol{A}$. $|\psi|^2$ is proportional to the density of superconducting electrons. Additionally, α and β are phenomenological parameters related to superconducting properties that we will discuss later, φ is the scalar potential, σ_n is the normal conductivity, Γ is the phenomenological rate of relaxation of ψ, and $e_s=2e$ and $m_s=2m$ are the total

charge and total effective mass of a Cooper pair, respectively. The TDGL equations are subject to boundary conditions:

$$\left(i\hbar\nabla\psi + \frac{e_s}{c}\boldsymbol{A}\psi\right)\cdot\boldsymbol{n} = 0, \tag{3}$$

$$\nabla\times\boldsymbol{A}\times\boldsymbol{n} = \boldsymbol{H}_a\times\boldsymbol{n}, \tag{4}$$

$$\left(\nabla\varphi + \frac{1}{c}\frac{\partial\boldsymbol{A}}{\partial t}\right)\cdot\boldsymbol{n} = 0, \tag{5}$$

where $\boldsymbol{n}$ is the outward normal vector to the boundary surface, and $\boldsymbol{H}_a$ is the applied magnetic field. Equation (3) ensures no current will flow out of the superconducting domain. Noting that $\boldsymbol{E} = -\nabla\phi + \frac{1}{c}\frac{\partial\boldsymbol{A}}{\partial t}$, Eqs. (4) and (5) are standard electromagnetic interface conditions with an applied magnetic field.

The parameters α, β, and Γ are temperature-dependent quantities. While they were originally introduced as phenomenological constants by Ginzburg and Landau, they can be derived from microscopic theories using the time-dependent Gor'kov equations [36]. This microscopic derivation relates these parameters to well-defined, experimentally observable material properties. The approximate material dependencies are given by Kopnin [37]:

$$\alpha(\nu(0), T_c, T) \approx \nu(0)\left(1 - \frac{T}{T_c}\right), \tag{6}$$

$$\beta(\nu(0), T_c, T) \approx \frac{7\zeta(3)\nu(0)}{8\pi^2 T_c^2}, \tag{7}$$

$$\Gamma(\nu(0), T_c) \approx \frac{\nu(0)\pi\hbar}{8T_c}, \tag{8}$$

where $\nu(0)$ is the Fermi-level density of states, T_c is the superconducting critical temperature, and T is the temperature; ζ is the Riemann zeta function. Using spatially varying values for $\nu(0)$, T_c, and T in Eqs. (6)–(8) gives nonuniform profiles for α, β, and Γ. This framework allows us to simulate the impact of material defects, such as Sn islands, on vortex nucleation. It is useful to introduce two other derived quantities, namely, the Ginzburg-Landau parameter κ and the thermodynamic critical field H_c. The Ginzburg-Landau parameter, $\kappa = \frac{\lambda}{\xi}$, relates the London penetration depth λ to the superconducting coherence length, ξ. These quantities can be expressed as functions of α and β [38]:

$$\kappa^2 = \frac{m_s^2 c^2 \beta}{2\pi\hbar^2 e_s^2}, \tag{9}$$

$$H_c^2 = \frac{4\pi\alpha^2}{\beta}. \tag{10}$$

The superheating field is related to these two quantities. Transtrum *et al.* [39] give an asymptotic expression for H_{sh} in the large κ limit:

$$\frac{H_{sh}(\kappa)}{\sqrt{2}H_c} \approx \frac{\sqrt{10}}{6} + \frac{0.3852}{\sqrt{\kappa}}. \tag{11}$$

The κ of Nb_3Sn is approximately ∼26, placing it solidly in the large κ limit, so Eqs. (6)–(11) accurately estimate the superheating field for Nb_3Sn directly from $\nu(0)$ and T_c.

The superheating field is a material-specific quantity defined for perfect materials and surfaces. When geometric or stoichiometric defects induce vortex nucleation at a field less than H_{sh}, it is a sample-specific phenomenon. Therefore, we define the sample-dependent field, H_{vort}, as the threshold for vortex nucleation of a specific (simulated) sample. For a uniform surface with no defect, $H_{vort} = H_{sh}$. In the presence of defects, the ratio H_{vort}/H_{sh} quantifies the reduction on the maximum field that the sample can sustain.

The TDGL equations have several important limitations in the context of SRF modeling. First, the equations are only quantitatively valid for temperatures near T_c, but are generally believed to be qualitatively faithful throughout the superconducting state. Next, the equations implicitly assume gapless superconductivity, as the singularity in the density of states for a gapped superconductor prevents the expansion of the free energy in powers of the energy gap [38]. The gapless condition can be lifted with the use of a generalized version of TDGL proposed by Kramer and Watts-Tobin [40], and future work may include implementing these equations. It is also worth noting that Proslier *et al.* [41] found evidence of gapless superconductivity in the surface of some Nb SRF cavities due to Nb oxides. Additionally, Gurevich and Kubo [42,43] have found a generic lowering of the energy gap and broadening of the near-gap density of states under typical SRF operating conditions. We argue that these findings further justify our use of TDGL for SRF applications. Additionally, the computational cost makes more detailed models prohibitively expensive, so TDGL strikes a reasonable balance between fidelity and accuracy. Because of these limitations, however, we only limit ourselves to drawing qualitative conclusions and making *relative* comparisons between different systems.

We solve the TDGL equations using finite-element methods. Most of the simulations were performed using COMSOL's general form partial differential equation solver [44], following the two-domain method laid out by Oripov and Anlage [45]. The fully embedded Sn island simulations were solved using the open-source PYTHON package FENICS [46] with the TDGL weak form originally derived by Gao and Sun [47]. We apply periodic boundary conditions in the X and Y directions of the domains, and a constant field oriented in the X direction is applied to the top surface of the domain. For the plots of two-domain simulations, the solid-filled regions are the superconductors, and everything else is vacuum. All simulations were run on the HPC cluster at Brigham Young University.

In practice, we solve a nondimensionalized version of Eqs. (1)–(5) [48] in which all of the physical constants are absorbed into the fields, and only factors of κ and dimensionless analogs of α, β, and Γ remain. Dimensionless values of α, β, and Γ are expressed relative to their corresponding values for Nb_3Sn. Similarly, Eq. (9) suggests that the value of κ ought to be determined by the reference value for β; however, numerical considerations motivate other choices. In most cases (except where explicitly stated otherwise) simulations use $\kappa = 10$ as the bulk value, which remains within the large κ limit [and thus Eq. (11) is still valid] but is smaller than the actual κ of Nb_3Sn (∼26). Large κ leads to simulations with extremely separated length scales that are both technically challenging and computationally expensive. To capture vortex nucleation, the full domain must span several penetration depths, while the element size of the meshes needs to be smaller than the coherence length. A mesh that produces good

solutions for $\kappa = 10$ would need ∼17 times as many elements to produce a similar quality simulation with $\kappa = 26$, and the total simulation time would be over 100 times as long.

Using smaller values of κ introduced controlled approximations into our simulations. As mentioned above, Eq. (9) shows that κ is determined by the value of β, and is independent of α. Referring to Eqs. (6) and (7), at low temperature, decreasing κ is roughly equivalent to increasing the effective T_c of the material. This also means that we are decreasing the value of Γ, but since Γ is a relaxation rate it will only affect the dynamics of the simulation and will have little to no effect on critical fields. So, using $\kappa = 10$ instead of 26 means effectively simulating a material that has the same density of states as Nb_3Sn, but a T_c that is a factor of 2.6 larger. From Eq. (10), H_c is therefore also a factor of 2.6 larger, and thus the corresponding H_{sh} calculated with Eq. (11) is strictly larger. Due to our definition of H_{vort}, there exists a limiting process for any defect in which $H_{vort} \to H_{sh}$. As a result of this, we argue that any given estimate for H_{vort} using $\kappa = 10$ will be strictly larger than the corresponding value for $\kappa = 26$, and the $\kappa = 26$ simulations that we did run corroborate this assertion. In summary, using $\kappa = 10$ allows simulations of superconductors within the large κ limit without the significant additional computational costs incurred by using $\kappa = 26$; while doing so does mean the simulated material is no longer exactly Nb_3Sn, the resulting H_{vort} estimates are still valuable, as they may be treated as upper bounds to the true $\kappa = 26$ values.

III. RESULTS AND DISCUSSION

A. General Nb_3Sn surface stoichiometry

1. *Experiment: Spatial distribution and characterization of* Nb_3Sn *stoichiometries*

Nb_3Sn stoichiometric inhomogeneities are more likely to form at specific regions throughout Nb_3Sn films grown via vapor deposition. For instance, Sn-deficient regions are preferentially located at (1) the intermetallic interface, (2) regions further from grain boundaries, and (3) at the film surface. The relationship between the grain boundary density and Sn stoichiometry is important because it impacts the film composition at all depths. For all three growth recipes, we observe the formation of "abnormal" Nb_3Sn grains that are large, smooth, and Sn deficient (Fig. S2, and Table SI of the Supplemental Material). These abnormal grains have been previously identified in literature as "patchy" and microscopy of film cross sections shows that these grains are also unusually thin and contain Sn deficiencies [11,16,30]. For this study, we focus on the stoichiometry of the first tens of nanometers into the Nb_3Sn surface and the different structural morphologies that form with varying Sn concentrations. While the Nb_3Sn surface does form a surface oxide upon exposure to atmosphere, we focus our discussion of the Nb_3Sn surface composition in terms of the relative Nb and Sn content. The XPS and AES data of the Nb_3Sn surface oxide are shown in Figs. S7 and S8.

To understand how the experimental growth conditions impact the Nb_3Sn surface stoichiometry, we must consider that the film surface morphology is driven by the relative Sn loss and accumulation rates that occur during the final cooldown steps of the growth procedure [Figs. 1(c) and 1(d)]. Throughout the vapor deposition growth procedure, adsorbed Sn vapor on the formed Nb_3Sn surface undergoes multiple diffusive processes including desorption, lateral diffusion, subsurface dissolution, and incorporation into the intermetallic unit cell [49,50]. The interplay and relative rates of these competing surface-mediated processes are primarily dictated by the Nb substrate temperature and Sn vapor flux above the surface. Therefore, the relative cooldown rates of the Nb and Sn heating sources can drastically impact the composition of the first few nanometers of the Nb_3Sn surface. An appreciable Sn vapor pressure is present while the Nb cavity drops below the temperatures required for Sn subsurface incorporation, between 800 °C and 900 °C, which will increase the density of Sn-rich and elemental Sn islands. On the other hand, a premature depletion of the Sn supply will result in excess Sn desorption from the Nb_3Sn surface. Post-deposition thermal treatments have been shown to deplete the Sn surface concentration (Fig. S8), not just by elemental Sn desorption, but from Sn segregating and desorbing from Nb_3Sn. The optimal ratio between the Nb and Sn temperature during the cooldown process is difficult to identify and is likely impossible to achieve experimentally.

For the UHV grown films [Recipes 1 and 2; Fig. 1(b)], the Nb and Sn cooldown process was rapid. The Nb source was cooled from 900 °C to below 300 °C in approximately 2 min. The main experimental differences in Recipe 1 are that the Nb cooldown was more gradual (reduced from 1100 °C to 900 °C in ∼20 min) and that the Sn temperature was slightly reduced about 2 min before the quenching of both Nb and Sn heating sources.

In contrast, the Nb_3Sn surface formed using the standard furnace deposition procedure (Recipe 3) had a much longer cooldown process. Since the Sn crucible was fully depleted, there was a period in which the Nb surface was heated with little to no Sn overpressure above the surface. This may have promoted the precipitation and desorption of Sn from the surface. However, we must also consider that this Nb_3Sn film was grown at a higher Sn flux and over a much longer period than in Recipes 1 and 2. Therefore, we expect fewer Sn-deficient regions within the first 100 nm of the Recipe 3 Nb_3Sn film. Globally, EDS analysis of the Recipe 3 Nb_3Sn film shows that the overall film is Sn rich, with the regular Nb_3Sn grains containing an estimated 26 at.% Sn (Fig. S6). Despite the higher Sn content, we still observe large, abnormal Nb_3Sn grains in the Recipe 3 film that are indicative of Sn deficiencies. These features will be discussed in Sec. III C 1 of the Results and Discussion.

2. *Theory: Effect of global* Nb_3Sn *stoichiometry on SRF performance*

While the specific local features present in Nb_3Sn surfaces will certainly have their own effects on SRF performance metrics, some of which we discuss later in this paper, we first consider the impact of stoichiometry alone. Equations (6)–(11) provide a method for estimating the H_{sh} of a material from the Fermi-level density of states and T_c of the material. Using this method, we can directly estimate the effect that stoichiometry will have on H_{sh}. Sitaraman *et al.* [51] performed DFT calculations on A15 phase Nb-Sn

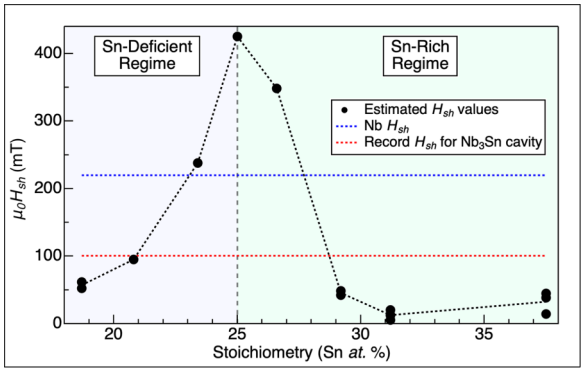

FIG. 2. H_{sh} as a function of Sn percentage. $\mu_0 H_{sh}$ is given in units of millitesla. The superheating field of pure Nb and the maximum field of the record Nb_3Sn cavity performance (documented in Posen *et al.* [6]) are also depicted for comparison.

systems, varying the concentration of antisite defects to estimate the Fermi-level density of states and T_c for different Sn at.%'s. Using these values with Eqs. (6)–(11), we estimate H_{sh} as a function of Nb_3Sn stoichiometry.

Figure 2 gives the bulk superheating field versus stoichiometry. While 25% Sn (perfect stoichiometry Nb_3Sn) has the expected value for $\mu_0 H_{sh}$ of ∼425 mT, off-stoichiometry samples exhibit significant performance degradation. Indeed, Fig. 2 demonstrates why Nb_3Sn is such a difficult material from which to engineer SRF cavities; even small deviations from the perfect stoichiometry can lead to significant reductions in H_{sh}, and by extension the limiting operating fields and maximum accelerating gradients. For example, a Sn stoichiometry of 23.4% cuts the expected H_{sh} nearly in half, and some Sn-rich compositions reduce H_{sh} nearly all the way to zero. The expected value of $\mu_0 H_{sh}$ for pure Nb is ∼220 mT (the blue line in Fig. 2), so not only do stoichiometric variations suppress the potential performance of Nb_3Sn surfaces, but it can even result in Nb_3Sn-coated Nb cavities that underperform elemental Nb. The record performance for a Nb_3Sn SRF cavity (the red line in Fig. 2) is an accelerating gradient of 24 MV/m, which corresponds to a peak magnetic field of ∼100 mT, well below even Nb's H_{sh}.

The H_{sh} values in Fig. 2 are valid for surfaces with a Sn composition that is uniformly distributed within the Nb_3Sn lattice. This assumption holds up well for many Sn-deficient compositions, as the $A15$ phase remains stable down to ∼17.5 Sn at.%; however, it is only stable for Sn-rich compositions up to ∼26% [52]. Compositions with higher Sn concentrations than this have not been observed in bulk, but they are known to appear locally near grain boundaries [9]. While the results in Fig. 2 could serve as an initial guess for the superconducting properties of some local feature, our calculations are only strictly applicable to surfaces that are nearly uniform on scales of several penetration depths (i.e., a few tenths of a micron). Real surfaces can exhibit both stoichiometric and structural variations on much smaller scales than this, which have specific impacts on vortex nucleation. Unfortunately, it is difficult to characterize samples on these scales. Experimental techniques such as EDS or XRD lack the sensitivity to resolve submicron-scale features, and so they must report weighted averages that may show a surface to be broadly Sn rich or Sn deficient. Such surfaces may be mostly good stoichiometry Nb_3Sn with many highly localized Sn-related defects. In these cases, the mechanisms for vortex nucleation are driven by the morphology of the specific defects rather than average stoichiometry. An example of one such surface defect is the presence of Sn islands embedded in the Nb_3Sn, which we cover in Sec. III B of this study. Additionally, variations in the surface geometry of the sample may further induce vortex nucleation. We explore an instance of this in Sec. III C, where we discuss the surface corrugation present on Sn-deficient grains.

B. Sn-rich regions on Nb_3Sn surface: Sn islands

1. Experiment: Partially embedded Sn islands

Sn-residue or Sn-rich regions due to elemental Sn islands or Sn-rich intermetallic phases (Nb_6Sn_5, $NbSn_2$), can often be found on Nb_3Sn surfaces [53,54]. The persistence and chemical identity of the Sn-rich residue is dependent on both the Nb temperature during and after Sn nucleates on the Nb_3Sn surface. Above 930 °C, we expect Sn to diffuse, predominantly through Nb_3Sn grain boundaries, to form the $A15$ Nb_3Sn structure [55].

For the Recipe 1 film, the accumulation of elemental Sn was observed on the surface and is shown in Fig. 3. The Sn islands were confirmed to not contain any detectable Nb with EDS analysis and are morphologically distinct from any Sn-rich intermetallic phase. We observe two distinct geometries for the Sn islands—larger irregular polyhedra and smaller tetrahedra. The SEM image in Fig. 3(a) shows an example of each Sn island geometry. The Nb $L\alpha$ EDS map [Fig. 3(b)] shows a lack of Nb EDS signal in the locations of each island. The Sn $L\alpha$ EDS map [Fig. 3(c)] shows a relative increase of Sn EDS signal at each Sn island. An EDS map depicting the relative Sn proportion is shown in Fig. 3(d) and was calculated by dividing the Sn $L\alpha$ EDS image by the sum of the Sn $L\alpha$ and Nb $L\alpha$ EDS images. In this relative Sn concentration map, the stoichiometric variations within the Nb_3Sn film are distinguishable from the more dramatic increase in Sn concentration due to the Sn islands. The diameter of the Sn islands varies, with the polyhedral islands ranging between 50 and 400 nm and the edge of the tetrahedral Sn islands typically ranging between 80 and 250 nm. Overall, the larger Sn islands conform to the polyhedral shape, with many appearing generally cubic.

Another varying aspect to these Sn islands is their topographic height. AFM images along with respective line scans are shown in Figs. 3(e)–3(h). Overall, the polyhedral island width is typically approximately three times as large as the protruding height. The tetrahedral islands tended to be more deeply embedded into the Nb_3Sn surface with the height only ∼25%−50% of the measured island width. The Sn islands overall have a greater diameter than topographic height which can be due to geometric asymmetry or a degree of embedment into the Nb_3Sn surface. It is worth noting that once these Sn islands form on the Nb_3Sn, removing them, via thermal desorption or incorporation into the Nb_3Sn lattice, is incredibly difficult. Annealing experiments have shown that the thermal stability of elemental Sn islands exceeds the thermal stability of Sn alloyed in the Nb_3Sn unit cell [56]. Thus, heating a

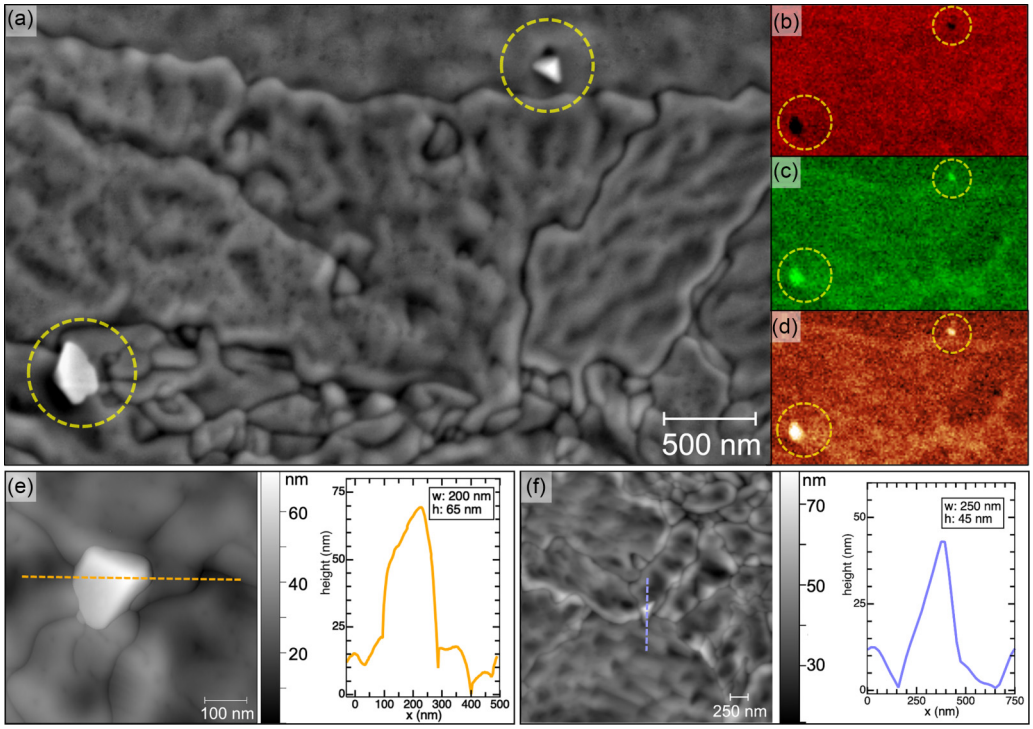

FIG. 3. Experimental data of polyhedral and tetrahedral Sn islands on Nb_3Sn surfaces grown using Recipe 1. SEM image (a) along corresponding EDS maps (b)–(d) show two Sn islands that are marked with the yellow dashed circles. AFM images of polyhedral and tetrahedral Sn island are shown in (e) and (f), respectively, along with corresponding line scans for each image. The inset textbox on each line scan denotes the width (w) and height (h) for each Sn island. Image sizes are denoted by scale bars. (a) SEM image, 4.17 μm×2.5 μm; SE2 detector, 7 keV; (b) Nb $L\alpha$ EDS map, 7 keV; (c) Sn $L\alpha$ EDS map, 7 keV; (d) calculated Sn($L\alpha$)/Nb($L\alpha$)+Sn($L\alpha$) EDS intensity proportion map; (e) AFM image of polyhedral Sn island, 600 nm×600 nm; (f) AFM image of tetrahedral Sn island, 5 μm×5 μm.

Sn-rich surface is likely to induce Sn deficiencies within the Nb_3Sn film at the temperatures necessary for Sn desorption to occur. This eliminates selective elemental Sn desorption through post-deposition thermal treatments as a viable option for reducing Sn-rich surfaces.

2. *Theory: Impact of island geometry and size on vortex nucleation*

We model Sn islands as idealized cubic and tetrahedral volumes embedded in the sample as shown in Figs. 4(a) and 4(d). Table II shows the values used for α, β, and Γ (relative to the corresponding values for Nb_3Sn) both inside and outside the islands as estimated using Eqs. (6)–(8). To determine the impact these Sn islands have on SRF performance, we estimate the lowest field at which vortices spontaneously nucleate, denoted by H_{vort}.

TABLE II. Parameter values used for Sn island simulations. Note that the α, β, and Γ values were defined relative to the respective values for Nb_3Sn to make them unitless for our simulations which use natural units. The values of $\nu(0)$ and T_c were calculated with DFT using the $A15$ phase for Nb_3Sn and the body-centered tetragonal phase for Sn and came from private correspondence.

Parameter	Nb_3Sn	Sn
$\nu(0)$ [states/(eV nm^3)]	101.78	16.8
T_c (K)	18	2.9
α/α_{Nb_3Sn} (unitless)	1	−0.029
β/β_{Nb_3Sn} (unitless)	1	3.907
Γ/Γ_{Nb_3Sn} (unitless)	1	0.803

Figure 4(b) shows one of our simulations for a cubic Sn island with side length λ (where for Nb_3Sn, $\lambda =\sim 100$ nm). In this case we found that $H_{\text{vort}} = 322.59$ mT, which is ∼24.2% lower than the superheating field for Nb_3Sn, $\mu_0 H_{\text{sh}} = 425$ mT. As discussed in Sec. II B, the κ for this simulation was 10, but for this size of island we ran another simulation with $\kappa = 26$, and found $H_{\text{vort}} = 304.73$ mT, which is ∼30% lower than the Nb_3Sn H_{sh}; this agrees with our earlier assertion that our $\kappa = 10$ simulation results may be treated as upper bounds (or lower bounds in terms of percentage decreases).

It is instructive to compare the impact of a localized Sn island to that of average stoichiometry. The volume-averaged Sn concentration of this simulation is given by

$$\text{Sn at.\%} = \frac{V_{\text{Sn}}}{3V_{\text{Nb}} + V_{\text{Sn}}}, \tag{12}$$

where V_{Sn} is the volume of the region containing Sn and V_{Nb} is the volume of the region containing Nb. In the case of Fig. 4, $V_{\text{Sn}} = 32.5\lambda^3$ and $V_{\text{Nb}} = 31.5\lambda^3$, resulting in a Sn at.% of ∼25.6%. From Fig. 2, we see that the expected $\mu_0 H_{\text{sh}}$ for a surface with a uniform Sn concentration of 26.5% is about 348 mT, which is only 18% lower than the Nb_3Sn H_{sh} of 425 mT. This means that surfaces with localized stoichiometric defects, such as the one from Fig. 3, may

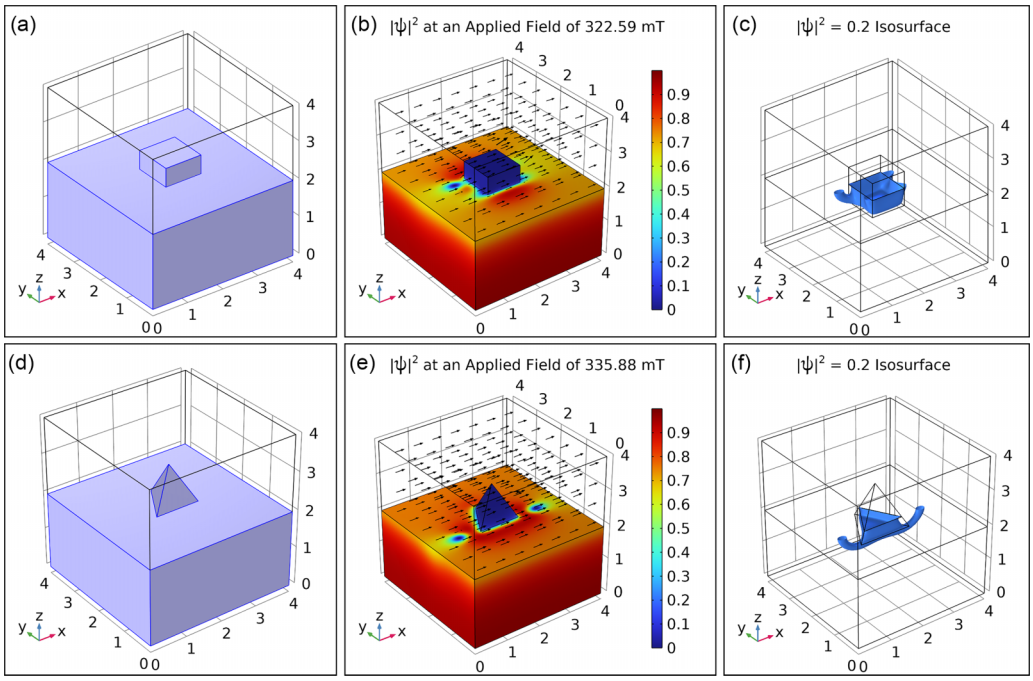

FIG. 4. (a) Simulation geometry of cubic Sn islands. Half of the cubic island is embedded below the surface. We also simulated some islands which were fully embedded, with the top surface of the cube flush with the Nb_3Sn surface (not pictured). (b) A plot of $|\psi|^2$ at an applied field of 348.25 mT. The black arrows show the direction of the magnetic field in the vacuum. (c) An isosurface of $|\psi|^2 = 0.2$ showing the shape of the vortex during nucleation. (d) Simulation geometry of tetrahedron Sn islands. Approximately half of the island's total volume is embedded below the surface. (e) A plot of $|\psi|^2$ at an applied field of 335.88 mT. The black arrows show the direction of the magnetic field in the vacuum. (f) An isosurface of $|\psi|^2 = 0.2$ showing the shape of the vortex during nucleation.

exhibit more significant SRF performance degradation than average stoichiometry alone would imply. In this case, the mechanism behind this degradation comes from Sn island-induced vortex nucleation that occurs 25%–30% below the Nb_3Sn H_{sh}.

We now consider the impact of island size on vortex nucleation. Table III reports the results of simulations with geometries similar to those in Fig. 4 with half of the island protruding above the surface, and the remaining half embedded beneath the surface. Larger islands lead to more significant decreases in H_{vort}. The largest island we simulated was a cube with side length 200 nm corresponding to an average Sn at.% of 30%. A uniform surface with a 30 at.% Sn will have a $\mu_0 H_{sh}$ of around ∼24.6 mT (see Fig. 2), which is an ∼94% decrease relative to the pure Nb_3Sn H_{sh}. Comparatively, the 200-nm side length cubic Sn islands only led to a 29.2% decrease. Thus, relative to uniform surfaces with the same at.% Sn, small Sn islands produce more significant drops in H_{vort} while larger Sn islands produce less significant drops in H_{vort}. An important caveat to this analysis is that the calculated Sn concentration of a simulation depends on both the total volume of the superconducting domain as well as the size of the island. We have chosen our domain size such that it falls within the range of reasonable resolutions for experimental techniques which can estimate material composition, such as EDS. The lateral and surface sensitivity of EDS is material dependent and has a complicated depth dependence which makes it difficult to estimate exactly, but it can reasonably be assumed to fall within a range of several hundred nanometers. Our simulation domains span ∼400 nm, and so the Sn at.% estimates of the compositions of these domains give a rough approximation for the local compositions of similar Sn islands measured experimentally.

We next consider cubic Sn islands fully embedded in the surface, with the top surface of the cube flush with the surrounding Nb_3Sn bulk. These simulations were performed

TABLE III. Results of half-embedded Sn islands.

Cubic island side length (nm)	$\mu_0 H_{vort}$ (mT)	% decrease from Nb_3Sn H_{sh}	Estimated Sn at.%	% decrease from Nb_3Sn H_{sh} for a uniform surface with equal Sn at.%
50	343.4	19.2%	25.07%	0.79%
100 ($\kappa = 10$)	322.59	24.2%	25.59%	6.68%
100 ($\kappa = 26$)	304.73	28.3%	25.59%	6.68%
200	300.9	29.2%	30.0%	94.21%

TABLE IV. Results of fully embedded Sn islands.

Cubic island side length (nm)	$\mu_0 H_{vort}$ (mT)	% decrease from H_{sh}	Estimated Sn at.%	% decrease from Nb_3Sn H_{sh} for a uniform surface with equal Sn at.%
50	313.65	26.2	25.07	0.79
100	274.55	35.4	25.6	6.68
200	228.65	46.2	30.77	96

using FENICS and the weak formulation derived by Gao and Sun [47] and our results are listed in Table IV. Similar to the half-embedded case, larger islands produce larger decreases in H_{vort} overall but have a smaller decrease relative to the Sn at.%, while smaller islands have smaller overall values with larger increases relative to the Sn at.%. It is notable that this fully embedded case reduces H_{vort} more than in the half-embedded case. We conjecture this is because the part of the island which is above the surface in the half-embedded case goes completely normal conducting, and so there is no magnetic field screening in that region. Therefore, from the perspective of the magnetic field, this part of the island is no different than vacuum, and so the island appears to have a smaller effective volume than their fully embedded counterparts. This smaller effective volume leads to lower H_{vort} values in the half-embedded islands.

Finally, we also considered a single tetrahedral Sn island. In this case we used a regular tetrahedron with an edge length of ∼150 nm, with roughly half of the total volume beneath the surface. Our result for $\kappa = 10$ is shown in Figs. 4(e) and 4(f). We found that for this case, $\mu_0 H_{vort} \approx 335.88$ mT, which is ∼26.9% lower than the Nb_3Sn H_{sh}. Notably, the total volume of this island is less than half the total volume of our cubic island with a side length of 100 nm. Even in the cubic case, the vortices tended to nucleate off the corners of the cube, so this result seems to imply that the smaller opening angle of the vertex of the tetrahedron more effectively nucleates vortices than the cube shape, resulting in a lower H_{vort}. We also simulated this island geometry for $\kappa = 26$, for which we found $\mu_0 H_{vort} \approx 304.58$ mT, approximately 28.3% lower than the expected H_{sh}.

C. Sn-deficient Nb_3Sn surfaces: Corrugations

1. Experiment: Formation of surface corrugations resulting from Sn loss

As was discussed in Sec. III A 1, the "abnormal," large Nb_3Sn grains contained some degree of Sn-deficient stoichiometries throughout the grain volume. However, the Sn composition within the first 100 nm drastically influences vortex nucleation. To assess the Nb_3Sn grain properties, we turn to structural morphology to augment our compositional characterization. SEM images of an abnormal, large grain formed from each film recipe are shown in Fig. 5. On the Recipe 1 film in Fig. 5(a), there are sporadically distributed 10-nm-sized pores on the surface. These pores were found on all of the Nb_3Sn films but were difficult to visualize with SEM with beam voltages exceeding 7 kV.

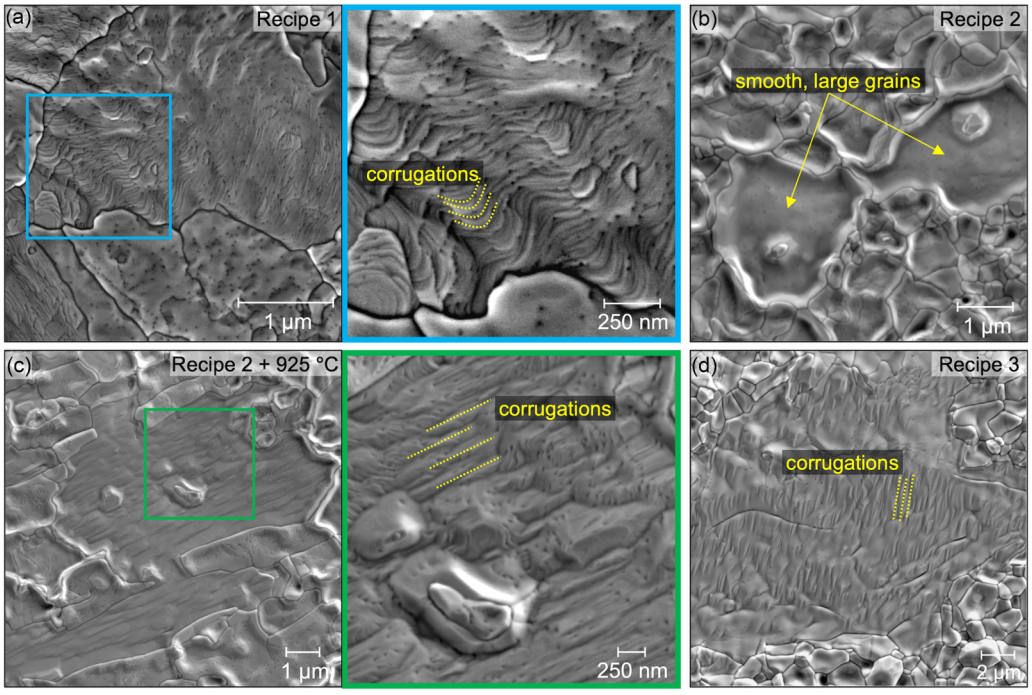

FIG. 5. SEM images of Nb_3Sn surfaces grown on polycrystalline Nb substrates with varying Sn deposition conditions. Image sizes are denoted by scale bars. (a) Recipe 1, UHV growth, 1.7 nm/min Sn flux, inset SEM area denoted with blue box, InLens detector, 3 kV; (b) Recipe 2, UHV growth, 4.2 nm/min Sn flux, SE detector; (c) Recipe 2+60-min UHV anneal at 925 °C, UHV growth, 4.2 nm/min Sn flux, SE detector; (d) Recipe 3, furnace growth, 3.8 nm/min Sn flux, SE detector.

For the UHV grown films, the surface area distributions of the abnormal Sn-deficient grains were comparable (Table SI). The main morphological distinction between the Recipe 1 and 2 films was that the Recipe 1 grains formed periodic corrugations [Fig. 5(a)], whereas the Recipe 2 large grains were smooth and absent of these features [Fig. 5(b)]. The corrugations on the Recipe 1 grains are periodic, with the peaks typically separated by 30–50 nm. The depth of the corrugations varies as well; the depth is highly unlikely to exceed the peak width. Not all of the large grains in Recipe 1 are corrugated; roughly 50% of the abnormal, Sn-deficient grains exhibited this corrugated surface morphology. There does seem to be a minor correlation between the grain area and the likelihood of forming surface corrugations. This may suggest that the formations of surface corrugations indicate a more egregious Sn deficiency, potentially for Nb_3Sn grains with close to the minimum 18 Sn at.% for the $A15$ structure.

For the abnormal, Sn-deficient grains formed using the Recipe 2 surface, the only distinguishable features were the nanopores and sporadic Sn-rich aggregates. The lack of corrugated grains on the large Recipe 2 Nb_3Sn grains (grown at a higher Sn flux) support that the formation of these corrugations is related to the Sn composition within the first 100 nanometers of the surface. If the formation of surfaces corrugations was only dependent on the Nb_3Sn grain surface area, we would expect at least some of the Recipe 2 grains to contain corrugations since the surface area distributions were not significantly different from Recipe 1 (Table SI). It is possible that the more rapid cooldown process used in Recipe 2 may have prevented Sn loss from the surface.

To test whether the corrugations are indicative of (1) an overall Sn deficiency based on the large grain area or (2) Sn deficiencies within the first 100 nanometers of the surface, we conducted post-deposition annealing experiments on the Recipe 2 Nb_3Sn film (AES data in Fig. S8). An SEM image of the Recipe 2 Nb_3Sn film that was annealed at 925 °C to induce Sn loss is shown in Fig. 5(c). Many of the large, abnormal grains now contain corrugations that appear shallower and more widely separated than the corrugations that were formed on the Recipe 1 film. During any Nb_3Sn annealing without a considerable Sn overpressure, Sn desorption dominates over any other diffusion processes [54,56]. Therefore, we can associate these corrugations with a Sn deficiency *specifically* within the first few nanometers of the surface.

Finally, Fig. 5(d) shows a large grain on the furnace grown (Recipe 3) Nb_3Sn film. We observe the shallow corrugations on the grain surface, similar to those formed on the annealed Recipe 2 film [Fig. 5(c)]. These corrugations may be symptomatic of substantial Sn loss from the Nb_3Sn surface. These observed corrugations can serve as a highly surface sensitive structural indicator of severe Sn deficiencies.

2. *Theory: Simulations of corrugated Sn-deficient* Nb_3Sn *surfaces*

We now model the effects that the corrugation geometry has on SRF performance. As a preface to the following discussion, it is important to note that the grains exhibiting these structures tend to be Sn deficient. We can see from Fig. 2 that for 18–24 Sn at.%, this stoichiometry already exhibits a 50%–80% drop in the expected H_{sh} based on the Sn

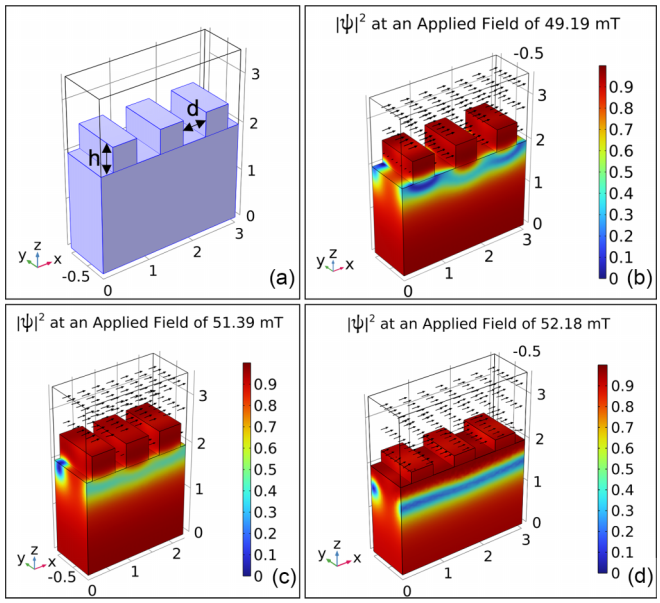

FIG. 6. (a) The geometry used for our corrugation simulations. The solid-filled region is the superconductor, with vacuum in the rest of the domain. Periodic boundary conditions are applied to the outer surfaces in the X and Y directions, and the external field is applied to the top surface of the vacuum domain. The distance labeled by h is the height of the ridges, and the distance labeled by d is the distance between them. (b)–(d) Plots of $|\psi|^2$ during vortex nucleation at different applied fields for different corrugation spacings and heights. The black arrows show the direction of the magnetic field in the vacuum. (b) has $h = 50$ nm, $d = 50$ nm. (c) has $h = 50$ nm, $d = 25$ nm. (d) has $h = 25$ nm, $d = 50$ nm.

deficiency alone. However, as we will demonstrate, the presence of these geometric corrugations has the potential to degrade this performance even further. We use an idealized geometry shown in Fig. 6(a), varying the height (h) and spacing (d) between the corrugations. This geometry unambiguously defines heights and widths for the corrugations while ignoring potential secondary effects due to curvature. Our primary goal with this part of the study is to qualitatively demonstrate some of the effects that the surface geometry of these corrugations has on SRF performance. Future work may include a more extensive study of the many different geometric factors at play in these simulations. Because of the periodic boundary conditions, these simulations are an infinite series of "boxlike" ridges, which approximate the local shape of the observed corrugations. For the same reasons discussed in Sec. II B, these simulations all use $\kappa = 10$, and the following H_{vort} estimates should be treated as upper bounds to the true values. For the purposes of estimating the critical field values, we assumed the corrugations to have a uniform composition of 18.7 Sn at.%, resulting in a superheating field of $\mu_0 H_{sh} = 57.1$ mT (see Fig. 2).

In our first corrugation simulations, we used ridges with heights and widths of 50 nm and ran two different simulations: one where the ridges have a 50-nm separation distance [shown in Fig. 6(b)] and the other with a 25-nm separation distance [Fig. 6(c)]. We find that the corrugations lead to a meaningful drop in H_{vort}, with the corrugations shown in Fig. 6(b)

producing an estimated $\mu_0 H_{\text{vort}} \approx 49.19$ mT, which is an $\sim$13.8% decrease below H_{sh}. The corrugations in Fig. 6(c) have an $\mu_0 H_{\text{vort}} \approx 51.39$ mT, a 10% decrease below H_{sh}. The vortex nucleation in this case happens because the ridges act as nucleation sites, with vortices having a much easier time entering the thin ridge. In addition to this, these ridges also exhibit some field enhancement, an effect where the Meissner effect pushing the field out of the material leads to field lines "bunching" up near the outer surface of geometric defects, leading to "enhanced" field magnitude near the defect surface. In this case, the local magnetic field magnitude is slightly larger than the applied field above each ridge, which further improves the possibility of vortex nucleation. The closer spaced corrugations led to a smaller decrease in H_{vort} because the field enhancement is smaller, as well as the surface appearing slightly closer to a flat surface.

We also simulated corrugations with a width of 50 nm and a height of 25 nm, as shown in Fig. 6(d). In this case the smaller ridges produced less field enhancement and were less strong nucleation sites, so the resulting $\mu_0 H_{\text{vort}}$ estimate was 52.18 mT. This is $\sim$8.5% lower than the expected value of H_{sh}, meaning that shallower corrugations have a less pronounced effect on vortex nucleation.

IV. CONCLUSION

In this work, experimental and theoretical results address how deviations in Nb_3Sn stoichiometry can manifest in distinct surface morphologies that have varying impacts on SRF performance. Experimentally, we demonstrate some of the limitations of characterizing Nb_3Sn by relying on global Sn atomic percentage estimates from experimental methods such as XRD or EDS. Not only does the Sn concentration vary drastically as a function of film depth, but the Nb_3Sn surface can contain drastically different surface morphologies with the same estimated chemical makeup. For example, a Sn-rich surface can manifest in micron-diameter Sn residue or sub-100-nm Sn particles that are difficult to characterize using the higher beam voltages ($\geqslant$10 kV) commonly used during SEM/EDS analysis of Nb_3Sn films. Simulated results of the impact of Sn island geometry on vortex nucleation show that smaller Sn islands will nucleate a vortex at a lower applied field as compared to a uniform flat Nb_3Sn surface with the same global Sn at.%. Conversely, we conclude that introducing a larger Sn island has a smaller than expected drop in the vortex nucleation field (H_{vort}) based on a uniform composition, though our estimated values for H_{vort} were still lower than the corresponding values for the small islands. For the Sn-deficient Nb_3Sn grains, we experimentally show that the Nb_3Sn surface develops a corrugated topography that may be used to identify Sn loss within the first few nanometers of the Nb_3Sn surface. While the simulation results show that bump corrugation geometries only minorly contribute to the vortex nucleation field reduction that already occurs on flat, uniformly Sn-deficient Nb_3Sn surfaces, these corrugations may serve as an identifying characteristic of extensive Sn loss from Nb_3Sn. Utilizing structural features to characterize Nb_3Sn surface stoichiometry can compensate for the experimental challenges associated with accurately chemically probing the first 100 nanometers of the Nb_3Sn surface.

Overall, these results demonstrate that local structural differences significantly impact superconducting properties of cavity surfaces, even on length scales smaller than the sensitivities of experimental techniques, such as EDS. The simulations in this study were performed using a smaller Ginzburg-Landau parameter of 10 than the true value of 26 for Nb_3Sn. While this choice was mostly due to technical constraints, our simulations still fall within the same "large κ" regime as Nb_3Sn. Choosing a smaller value for κ is effectively equivalent to increasing the T_c while holding the Fermi-level density of states constant, and the ultimate result of this is that our H_{vort} predictions are likely overestimates of the true values. The $\kappa = 26$ results we did obtain agree with this, as the simulations for a 100-nm Sn island at $\kappa = 26$ had a 28.3% vortex nucleation field reduction compared to 24.4% at $\kappa = 10$. The biggest drop in H_{vort} relative to the Nb_3Sn H_{sh} we estimated was 46.2% for the fully embedded 200-nm island, so the true impact of such an island is likely an even larger drop in performance. This island is still relatively small compared to the scale of many of the defects in Nb_3Sn samples, so it is plausible that larger instances of Sn islands are contributing to the performance limitations which have plagued Nb_3Sn cavities to date.

Future studies should involve simulating more sizes of Sn islands, particularly smaller ones, that may further illuminate performance degradations which can occur for even surfaces which may appear only minimally Sn rich. Also, larger, longer-term simulations done at $\kappa = 26$ may help determine the specific thresholds for vortex nucleation. Collaborative experimental-theory efforts should also be dedicated to understanding how the Nb_3Sn surface oxide, alternative Nb-Sn phases (Nb_6Sn_5, $NbSn_2$), and other film properties affect the expected SRF behavior. It would also be beneficial to simulate how the stoichiometric variations at non-surface-specific features, such as grain boundaries, further contribute to variations in SRF performance [27]. For example, building upon previous studies of vortex nucleation at Nb_3Sn grain boundaries by Carlson *et al.* [8], the SRF performance can be directly correlated to experimental scanning transmission electron microscopy and electron energy loss spectroscopy data of Sn-rich subsurface features.

There currently exists a significant gap between theoretical and experimental Nb_3Sn SRF optimization efforts. Many Nb_3Sn surface defects have been observed throughout the SRF community and have proven immensely difficult to prevent or remove during the fabrication process. Experimentally, it is likely impossible to form a defect-free Nb_3Sn surface on a Nb SRF cavity using the vapor deposition procedure. Despite this, there is relatively little prior theoretical work specifically modeling the effect of the wide variety of observed material defects. In order to continue the monumental progress made towards improving the quality of vapor-deposited Nb_3Sn films, we need to know which stoichiometric defects have the largest impact on accelerating gradients and prioritize reducing their incidence. We argue experiment-informed theoretical models are the best way to determine the impact of defects, since it is generally impossible to isolate microscopic defects for direct measurement. This work provides a systematic approach to close the experiment-theory gap in the SRF community. We developed an intuitive framework to

create predictive models which combine experimental characterizations of defects in Nb_3Sn surfaces with theoretical methods that model the interaction of these defects with applied magnetic fields. These models allow us to estimate how specific submicron-scale defects attenuate high-field SRF performance. While the results we report in this work include specific insights about the growth and impact of Sn islands and Sn-deficient surfaces, our methods provide a general framework for future studies. This study as well as future ones like it will help to guide the development of improved Nb_3Sn fabrication procedures that can enable the next generation of SRF cavities.

ACKNOWLEDGMENTS

We thank Dr. Alexander Filatov of the University of Chicago for help with the x-ray diffraction measurements and Dr. Nathan Sitaraman for conducting DFT calculations for the $\nu(0)$ and T_c values for the $A15$ phase for Nb_3Sn and the body-centered tetragonal phase for Sn. This work was supported by the U.S. National Science Foundation under Award PHY-1549132, the Center for Bright Beams. The infrastructure and facilities from the NSF Materials Research Science and Engineering Center (MRSEC) at the University of Chicago (under Grant No. NSF-DMR-2011854) are also acknowledged.

[1] P. C. Bhat *et al.*, Future high energy colliders and options for the U.S, J. Inst. **18**, P12007 (2023).

[2] C. Antoine, Materials and surface aspects in the development of SRF niobium cavities, in *EuCARD Editorial Series on Accelerator Science* (Warsaw, Poland, 2012).

[3] T. Proslier, J. Zasadzinski, L. Cooley, M. Pellin, J. Norem, J. Elam, C. Z. Antoine, R. A. Rimmer, and P. Kneisel, Tunneling study of SRF cavity-grade niobium, IEEE Trans. Appl. Supercond. **19**, 1404 (2009).

[4] D. Bafia, *Exploring and Understanding the Limitations of Nb SRF Cavity Performance*, Ph.D. thesis, Illinois Institute of Technology, 2020.

[5] A. Godeke, Nb_3Sn *for Radio Frequency Cavities* (Lawrence Berkeley National Laboratory, 2006).

[6] S. Posen, J. Lee, D. N. Seidman, A. Romanenko, B. Tennis, O. S. Melnychuk, and D. A. Sergatskov, Advances in Nb_3Sn superconducting radiofrequency cavities towards first practical accelerator applications, Supercond. Sci. Technol. **34**, 025007 (2021).

[7] R. Porter, D. L. Hall, M. Liepe, and J. T. Maniscalco, Surface roughness effect on the performance of Nb_3Sn Cavities, in *Proceedings of the LINAC2016, East Lansing, MI, USA* (Joint Accelerator Conferences Website (JACoW), 2016), pp. 129–132.

[8] J. Carlson *et al.*, Analysis of magnetic vortex dissipation in Sn-segregated boundaries in Nb_3Sn superconducting RF cavities, Phys. Rev. B **103**, 024516 (2021).

[9] J. Lee, Z. Mao, K. He, Z. H. Sung, T. Spina, S.-I. Baik, D. L. Hall, M. Liepe, D. N. Seidman, and S. Posen, Grain-boundary structure and segregation in Nb_3Sn coatings on Nb for high-performance superconducting radiofrequency cavity applications, Acta Mater. **188**, 155 (2020).

[10] S.-H. Oh, D. Seol, Y.-J. Jeong, S.-H. Na, J. Kim, W.-S. Ko, J. B. Jeon, and B.-J. Lee, Diffusion in A15 Nb_3Sn: An atomistic study, Acta Mater. **234**, 118050 (2022).

[11] Y. Trenikhina, S. Posen, A. Romanenko, M. Sardela, J.-M. Zuo, D. L. Hall, and M. Liepe, Performance-defining properties of Nb_3Sn coating in SRF cavities, Supercond. Sci. Technol. **31**, 015004 (2017).

[12] C. Becker, S. Posen, N. Groll, R. Cook, C. M. Schlepütz, D. L. Hall, M. Liepe, M. Pellin, J. Zasadzinski, and T. Proslier, Analysis of Nb_3Sn surface layers for superconducting radio frequency cavity applications, Appl. Phys. Lett. **106**, 082602 (2015).

[13] E. Viklund, J. Lee, D. N. Seidman, and S. Posen, Three-dimensional reconstruction of Nb_3Sn films by focused ion beam cross sectional microscopy, IEEE Trans. Appl. Supercond. **33**, 1 (2023).

[14] A. Godeke, A review of the properties of Nb_3Sn and their variation with A15 composition, morphology and strain state, Supercond. Sci. Technol. **19**, R68 (2006).

[15] Z. Sun, Z. Baraissov, R. D. Porter, L. Shpani, Y.-T. Shao, T. Oseroff, M. O. Thompson, D. A. Muller, and M. U. Liepe, Smooth, homogeneous, high-purity Nb_3Sn superconducting RF resonant cavity by seed-free electrochemical synthesis, Supercond. Sci. Technol. **36**, 115003 (2023).

[16] U. Pudasaini, G. V. Eremeev, J. W. Angle, J. Tuggle, C. E. Reece, and M. J. Kelley, Growth of Nb_3Sn coating in tin vapor-diffusion process, J. Vac. Sci. Technol. A **37**, 051509 (2019).

[17] P. Zhang, Y. Y. Lau, and R. M. Gilgenbach, Analysis of radio-frequency absorption and electric and magnetic field enhancements due to surface roughness, J. Appl. Phys. **105**, 114908 (2009).

[18] U. Pudasaini, C. Reece, and J. Tiskumara, Managing Sn-supply to tune surface characteristics of vapor-diffusion coating of Nb_3Sn, in *Proceedings of the 20th International Conference on RF Superconductivity* (Joint Accelerator Conferences Website (JACoW), US, 2021).

[19] J. Tiskumara, J. Delayen, U. Pudasaini, C. Reece, and G. Eremeev, Nb_3Sn coating of twin axis cavity for SRF applications, in *Proceedings of the 20th International Conference on RF Superconductivity, East Lansing, MI* (Joint Accelerator Conferences Website (JACoW), 2022).

[20] J. Tiskumara, J. Delayen, G. Eremeev, and U. Pudasaini, Lower temperature annealing of vapor diffused Nb_3Sn for accelerator cavities, in *Proceedings of the 5th North American Particle Accelerator Conference (NAPAC2022)* (Joint Accelerator Conferences Website (JACoW),2022).

[21] S. Burgess, J. Sagar, J. Holland, X. Li, and F. Bauer, Ultra-low kV EDS—A new approach to improved spatial resolution, surface sensitivity, and light element compositional imaging and analysis in the SEM, Microsc. Today **25**, 20 (2017).

[22] C. R. Brundle and B. V. Crist, X-ray photoelectron spectroscopy: A perspective on quantitation accuracy for composition analysis of homogeneous materials, J. Vac. Sci. Technol. A **38**, 041001 (2020).

[23] A. Cano, G. V. Eremeev, J. R. Zuazo, J. Lee, B. Luo, M. Martinello, A. Romanenko, and S. Posen, Selective thermal evolution of a native oxide layer in Nb and Nb_3Sn-coated SRF

grade Nb: An *in situ* XPS study, J. Phys. Chem. C **127**, 19705 (2023).
[24] S. Posen, N. Valles, and M. Liepe, Radio frequency magnetic field limits of Nb and Nb_3Sn, Phys. Rev. Lett. **115**, 047001 (2015).
[25] S. Keckert *et al.*, Critical fields of Nb_3Sn prepared for superconducting cavities, Supercond. Sci. Technol. **32**, 075004 (2019).
[26] H. Devantay, J. L. Jorda, M. Decroux, J. Muller, and R. Flükiger, The physical and structural properties of superconducting A15-type Nb-Sn alloys, J. Mater. Sci. **16**, 2145 (1981).
[27] M. M. Kelley, N. S. Sitaraman, and T. A. Arias, *Ab initio* theory of the impact of grain boundaries and substitutional defects on superconducting Nb_3Sn, Supercond. Sci. Technol. **34**, 015015 (2020).
[28] S. A. Willson, R. G. Farber, A. C. Hire, R. G. Hennig, and S. J. Sibener, Submonolayer and monolayer Sn adsorption and diffusion behavior on oxidized Nb(100), J. Phys. Chem. C **127**, 3339 (2023).
[29] R. G. Farber, S. A. Willson, and S. J. Sibener, Role of nanoscale surface defects on Sn adsorption and diffusion behavior on oxidized Nb(100), J. Vac. Sci. Technol. A **39**, 063212 (2021).
[30] J. Lee, S. Posen, Z. Mao, Y. Trenikhina, K. He, D. L. Hall, M. Liepe, and D. N. Seidman, Atomic-scale analyses of Nb_3Sn on Nb prepared by vapor diffusion for superconducting radiofrequency cavity applications: A correlative study, Supercond. Sci. Technol. **32**, 024001 (2018).
[31] G. Jiang *et al.*, Understanding and optimization of the coating process of the radio-frequency Nb_3Sn thin film superconducting cavities using tin vapor diffusion method, Appl. Surf. Sci. **643**, 158708 (2024).
[32] See Supplemental Material at http://link.aps.org/supplemental/10.1103/PhysRevResearch.6.043133 for additional details of film growth recipes 1-3 and supporting experimental characterization of the Nb_3Sn films.
[33] M. Ohring, *The Material Science of Thin Films* (Academic Press, San Diego, CA, 1992).
[34] C. B. Alcock, V. P. Itkin, and M. K. Horrigan, Vapour pressure equations for the metallic elements: 298–2500 K, Can. Metall. Q. **23**, 309 (1984).
[35] D. Hall, *New Insights into the Limitations on the Efficiency and Achievable Gradients in* Nb_3Sn *SRF Cavities, Dissertation*, (Cornell University, 2017).
[36] L. Gor'Kov and G. Eliashberg, Generalization of the Ginzburg-Landau equations for non-stationary problems in the case of alloys with paramagnetic impurities, Sov. Phys. JETP **27**, 328 (1968).
[37] N. Kopnin, *Theory of Nonequilibrium Superconductivity* (Oxford University Press, New York, 2001), Vol. 110.
[38] M. Tinkham, *Introduction to Superconductivity* (Courier Corporation, North Chelmsford, MA, 2004).
[39] M. K. Transtrum, G. Catelani, and J. P. Sethna, Superheating field of superconductors within Ginzburg-Landau theory, Phys. Rev. B **83**, 094505 (2011).
[40] L. Kramer and R. J. Watts-Tobin, Theory of dissipative current-carrying states in superconducting filaments, Phys. Rev. Lett. **40**, 1041 (1978).
[41] T. Proslier, J. F. Zasadzinski, L. Cooley, C. Antoine, J. Moore, J. Norem, M. Pellin, and K. E. Gray, Tunneling study of cavity grade Nb: Possible magnetic scattering at the surface, Appl. Phys. Lett. **92**, 212505 (2008).
[42] A. Gurevich and T. Kubo, Surface impedance and optimum surface resistance of a superconductor with an imperfect surface, Phys. Rev. B **96**, 184515 (2017).
[43] T. Kubo and A. Gurevich, Field-dependent nonlinear surface resistance and its optimization by surface nanostructuring in superconductors, Phys. Rev. B **100**, 064522 (2019).
[44] COMSOL Inc., *COMSOL Multiphysics* (COMSOL Inc., Burlington, MA, 2023).
[45] B. Oripov and S. M. Anlage, Time-dependent Ginzburg-Landau treatment of rf magnetic vortices in superconductors: Vortex semiloops in a spatially nonuniform magnetic field, Phys. Rev. E **101**, 033306 (2020).
[46] M. S. Alnæs, J. Blechta, J. Hake, A. Johansson, B. Kehlet, A. Logg, C. Richardson, J. Ring, M. E. Rognes, and G. N. Wells, The FEniCS project version 1.5, Arch. Numer. Software **3**, 9 (2015).
[47] H. Gao and W. Sun, A new mixed formulation and efficient numerical solution of Ginzburg–Landau equations under the temporal gauge, SIAM J. Sci. Comput. **38**, A1339 (2016).
[48] A. V. Harbick and M. K. Transtrum, A time-dependent Ginzburg-Landau framework for sample-specific simulation of superconductors for SRF applications, arXiv:2410.20078.
[49] C. T. Campbell, Ultrathin metal films and particles on oxide surfaces: Structural, electronic and chemisorptive properties, Surf. Sci. Rep. **27**, 1 (1997).
[50] D. R. Askeland, *The Science and Engineering of Materials* (Chapman Hall, Oxford, UK, 1996).
[51] N. S. Sitaraman, M. M. Kelley, R. D. Porter, M. U. Liepe, T. A. Arias, J. Carlson, A. R. Pack, M. K. Transtrum, and R. Sundararaman, Effect of the density of states at the Fermi level on defect free energies and superconductivity: A case study of Nb_3Sn, Phys. Rev. B **103**, 115106 (2021).
[52] J. P. Charlesworth, I. Macphail, and P. E. Madsen, Experimental work on the niobium-tin constitution diagram and related studies, J. Mater. Sci. **5**, 580 (1970).
[53] M. N. Sayeed, U. Pudasaini, C. E. Reece, G. V. Eremeev, and H. E. Elsayed-Ali, Properties of Nb_3Sn films fabricated by magnetron sputtering from a single target, Appl. Surf. Sci. **541**, 148528 (2021).
[54] M. N. Sayeed, U. Pudasaini, C. E. Reece, G. Eremeev, and E. H. Elsayed-Ali, Structural and superconducting properties of Nb_3Sn films grown by multilayer sequential magnetron sputtering, J. Alloys Compd. **800**, 272 (2019).
[55] E. Barzi, M. Bestetti, F. Reginato, D. Turrioni, and S. Franz, Synthesis of superconducting Nb_3Sn coatings on Nb substrates, Supercond. Sci. Technol. **29**, 015009 (2015).
[56] S. A. Willson, H. Lew-Kiedrowska, V. Do, and S. J. Sibener, Influence of Nb substrate morphology and atomic structure on Sn nucleation and early Nb_3Sn growth, Appl. Surf. Sci. **664**, 160272 (2024).